Aerodynamic noise from a poroelastic edge with implications for the silent flight of owls

Justin W. Jaworski† and N. Peake

Department of Applied Mathematics and Theoretical Physics, University of Cambridge,
Centre for Mathematical Sciences, Wilberforce Road, Cambridge CB3 0WA, UK

The interaction of a turbulent eddy with a semi-infinite poroelastic edge is examined with respect to the effects of both elasticity and porosity on the efficiency of aerodynamic noise generation. The scattering problem is solved using the Wiener–Hopf technique to identify the scaling dependence of the resulting aerodynamic noise on plate and flow properties, including the dependence on a characteristic flow velocity U. Special attention is paid to the limiting cases of porous-rigid and impermeable–elastic plate conditions. Asymptotic analysis of these special cases reveals parametric limits where the far-field acoustic power scales like U^6 for a porous edge, and a new finite range of U^7 behaviour is found for an elastic edge, to be compared with the well-known U^5 dependence for a rigid impermeable edge. Further numerical results attempt to address how trailing-edge noise may be mitigated by porosity and flexibility and seek to deepen the understanding of how owls hunt in acoustic stealth.

Key words: aeroacoustics, flow–structure interactions, swimming/flying

---

1. Introduction

Many owl species rely on bi-aural acoustic targeting to hunt their prey in acoustic stealth. Aeroacoustic measurements by Kroeger, Gruschka & Helvey (1972) and more recently by Sarradj, Fritzsche & Geyer (2011) indicate that owls can eliminate virtually all self-noise from about 1.6 to 10 kHz, a range of frequencies over which human audition is most sensitive. Therefore, the identification of the physical mechanisms by which the owl is able to achieve this noise reduction may have significant application to the development of quieter airframes and other aerodynamic structures where edge noise is prominent.

Owls are believed to fly silently as a result of three distinctive and unique physical features (Graham 1934): a soft downy coating on the upper wing surface, a comb of stiff feathers at the wing leading edge, and a fringe of flexible filaments at the trailing edges of the feathers and wing. The trailing edge is an unavoidable source of noise for aerodynamic structures in a fluid flow, and, thus, a large body of research has been developed to model and mitigate the noise due to the edge interaction with turbulent eddies in the boundary layer passing over it. Ffowcs Williams & Hall (1970) identified the dependence of radiated intensity due to a turbulent source near a rigid

† Email address for correspondence: J.W.Jaworski@damtp.cam.ac.uk

trailing edge on the fifth power of the flight speed, which has been well-supported by flight data (Crighton 1991). Further work by Howe (1978) extended consideration to the effects of the Kutta condition, forward flight, and source motion in a unified theory of rigid trailing-edge noise for low-Mach-number flows.

Strategies for passive edge-noise reduction have focused on modifications to the geometry, elasticity, and porosity of the edge itself. Geometric edge modifications in the form of sawtooth serrations have been investigated analytically (Howe 1991*a*,*b*), computationally (Sandberg & Jones 2011; Jones & Sandberg 2012), and experimentally (Dassen *et al.* 1996; Oerlemans *et al.* 2009; Moreau, Brooks & Doolan 2012; Chong, Joseph & Gruber 2013), motivated by the goal to reduce flow coherence along the edge to effect noise reductions. Despite the fact that noise reductions can indeed be achieved with edge serrations, the distinct differences noted between the experimental observations by Moreau *et al.* (2012) and Chong *et al.* (2013) and the predictions by the theory of Howe (1991*a*,*b*) for the overall magnitude and parametric trends of noise reduction with respect to the serration geometry underscore the need for further research to reconcile these controversies.

The use of geometric variations along the edge due to serrations or stiff brush inserts (see Herr & Dobrzynski 2005) is one of many ways outlined by Hayden (1976) to implement a variable impedance for a rigid trailing edge. The effects of trailing-edge compliance were first addressed by Crighton & Leppington (1970), who employed the Wiener–Hopf technique to identify a weaker sixth-power velocity dependence in the limit of heavy fluid loading for a sufficiently limp edge. This sixth-power velocity scaling is identical, but not physically related, to that of the surface dipole (Curle 1955). However, an examination of owl aeroacoustic data taken by Kroeger *et al.* (1972) led Lilley (1998) to hypothesize that the trailing-edge fringe washes out a hard edge condition, leading empirically to a sixth-order velocity dependence for radiated intensity.

The effects of trailing-edge elasticity have been investigated previously with respect to both the long-range transmission and scattering of bending waves (Crighton 1972; Cannell 1975, 1976; Howe 1992) and the scattering of turbulent sources (Howe 1993). In the latter case, for sufficiently low Mach numbers the radiated intensity is shown to become a function of the ratio of the incident and coincidence frequencies. The attenuation of noise via surface porosity has been considered in many different contexts, including absorptive wall coatings (Zwikker & Kosten 1949; Bliss 1982), bias flow sound absorbers (Hughes & Dowling 1990), and Helmholtz resonators coupled to a flow via evenly spaced apertures (Leppington 1990). The modelling of porosity by Rayleigh conductivity across apertures in a rigid frame has been shown by Leppington (1977) to lead to boundary conditions similar to the point-reacting compliant edge of Crighton & Leppington (1970). The Rayleigh conductivity approach to porosity modelling has also been demonstrated to reduce edge noise both theoretically, for example, due to a vortex passing a trailing edge with different porosity distributions (Howe 1979*a*), as well as computationally, as in the case of the sharp cusp on a leading-edge slat (Khorrami & Choudhari 2003). Howe (1998) combines the features of elasticity and porosity to examine the transmission of incident sound through an infinite poroelastic plate, but to the authors' knowledge such a model has not been used to examine the scattering of turbulent noise sources from a poroelastic trailing edge.

The present work seeks to evaluate the separate and combined influences of flexural elasticity and surface porosity on the scattering efficiency of a semi-infinite plate in the vicinity of a turbulent source. The poroelastic-plate equation of Howe (1998)
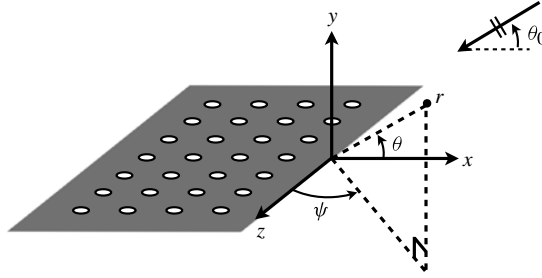
FIGURE 1. Schematic of the poroelastic half-plane and incident plane wave for the reciprocal acoustic scattering problem.

models the semi-infinite edge for small fractional open areas in terms of measurable physical quantities and permits the analysis of limiting cases such as zero porosity and perfect plate rigidity. The model equations are developed in §2 for the scattering of a source located far from a semi-infinite poroelastic plate, whose near-field solution furnishes the far-field sound due to a source near the plate by reciprocity arguments. The model equations are then formulated as a Wiener–Hopf problem in §3 and are solved exactly in §4 using the numerical kernel splitting approach of Peake (2004) to yield the acoustic amplification of the turbulent eddy due to the presence of the edge. Asymptotic splitting and evaluation of the Wiener–Hopf kernel carried out in §5 for the special cases of rigid (porous or impermeable) and elastic impermeable edges identify conditions where fifth-, sixth- and seventh-power dependences of aerodynamic noise on the characteristic flow velocity are predicted. Numerical predictions in §6 for the full poroelastic kernel are made based on the aeroacoustic measurements by Herr (2007) of trailing-edge brush inserts, and areas for potential improvements in noise reduction are suggested by the present theory.

2. Model problem

The semi-infinite poroelastic plate is represented by a plate model developed by Howe (1998), written in terms of the plate transverse displacement η and the displacement η_a of the fluid in the evenly spaced, circular apertures as illustrated in figure 1,

$$(1 - \alpha_H) \left\{ \bar{B} \nabla_{x,z}^4 + m \frac{\partial^2}{\partial t^2} \right\} \eta - \Delta p = 2\alpha_H R \rho_f \frac{\partial^2 \eta_a}{\partial t^2}. \tag{2.1}$$

The plate has specific mass m, and the effective plate stiffness $\bar{B} = [1 - 2\alpha_H \nu/(1-\nu)]B$ is written in terms of the plate flexural rigidity B, Poisson ratio ν, and fractional open area α_H. The fractional open area is defined by $\alpha_H = N\pi R^2$, where N is the number of circular apertures of radius R per unit area. Assuming the time dependence $e^{-i\omega t}$, the average fluid displacement in the apertures may be written as $\eta_a = -K_R \Delta p/(\pi \rho_f \omega^2 R^2)$ in terms of the pressure difference $\Delta p = p(x, 0^-, z) - p(x, 0^+, z)$ across the plate, the fluid density ρ_f, and the Rayleigh conductivity K_R, which must be determined by some external data or model. In the absence of a mean flow, the pressure is directly related to the velocity potential of the scattered field by the unsteady Bernoulli equation, $p = -\rho_f \partial\phi/\partial t$, and the Rayleigh conductivity for a circular aperture becomes $K_R = 2R$ (Rayleigh 1945, §306; Howe 1979b; Howe, Scott & Sipcic 1996). The validity of the poroelastic-plate model (2.1) for the present aeroacoustic problem

requires $\alpha_H^2 \ll 1$, $k_0 R \ll 1$ and $k_B R \ll 1$, where the *in vacuo* bending wavenumber is defined by $k_B \equiv (m\omega^2/\bar{B})^{1/4}$. These restrictions assert that the poroelastic-plate model is a first-order correction to account for the plate perforations, and that the length scales of disturbances incident upon or scattered by the apertures must be much larger than the aperture radius.

The sound observed in the acoustic far field due to a source near the poroelastic edge is determined by first solving the reciprocal problem, i.e. solving for the scattered field near the edge due to an incident plane wave from the far field, and by invoking the reciprocal theorem (Rayleigh 1945, § 294). The velocity potential of the incident plane wave from the far field is

$$\phi_0(\boldsymbol{x}) \sim \frac{e^{ik_0 r_0}}{r_0} \exp\left[-ik_0 \sin\psi_0 (x\cos\theta_0 + y\sin\theta_0) + ik_0 z\cos\psi_0\right], \tag{2.2}$$

as $r_0 \to \infty$ for finite $r = |\boldsymbol{x}|$, where in the fluid $k_0 = \omega/c_0$ and c_0 is the speed of sound. The velocity potential ϕ_0 represents the far-field acoustic wave emitted from a point source located at distance r_0 from the origin. Note that the time factor $e^{-i\omega t}$ has been suppressed, and ω is assumed to have a small, positive imaginary part to ensure convergence of the Fourier transforms. The kinematic boundary condition at the poroelastic surface requires

$$\left.\frac{\partial}{\partial y}(\phi_0 + \phi)\right|_{y=0} = \frac{\partial}{\partial t}\left[(1-\alpha_H)\eta(x,z) + \alpha_H \eta_a(x,z)\right], \tag{2.3}$$

where the right-hand side corresponds to the effective local displacement velocity, averaged over the solid and aperture portions of the plate.

The z-dependence set by the incident field, $\partial/\partial z = ik_0 \cos\psi_0$, enables the three-dimensional scattered field to be written as the solution to a two-dimensional Helmholtz equation,

$$\left(\nabla_{x,y}^2 + k^2\right)\phi = 0, \tag{2.4}$$

where $k \equiv k_0 \sin\psi_0$ is the reduced wavenumber.

It is convenient to non-dimensionalize the set of governing equations by introducing the coincidence frequency $\omega_c = (mc_0^4/\bar{B})^{1/2}$, the intrinsic fluid loading parameter $\epsilon = \rho_f k_0/(mk_B^2)$, and the vacuum bending wave Mach number $\Omega = (\omega/\omega_c)^{1/2} = k_0/k_B$. Denoting dimensionless variables by hats, the following scalings are employed:

$$\left.\begin{array}{ll} \eta = k_B^{-1}\hat{\eta}, & p = \rho_f \omega_c^2 k_B^{-2}\hat{p}, \quad \phi = \omega_c k_B^{-2}\hat{\phi}, \quad \omega = \omega_c \Omega^2, \\ R = k_B^{-1}\hat{R}, & K_R = k_B^{-1}\hat{K}_R, \quad t = \omega_c^{-1}\hat{t}, \quad (x,y,z) = k_B^{-1}(\hat{x},\hat{y},\hat{z}), \end{array}\right\} \tag{2.5}$$

and any parameters not shown are scaled using ω_c for inverse time and k_B for inverse length. Dropping the hats on the dimensionless quantities, the conditions for the valid use of the poroelastic-plate equation become $\alpha_H^2 \ll 1$, $\Omega R \ll 1$ and $R \ll 1$. The complete set of dimensionless equations for the scattering of an incident plane wave by a semi-infinite poroelastic plate becomes the following:

$$\phi_0(\boldsymbol{x}) = \frac{e^{i\Omega r_0}}{r_0} \exp\left[-i\Omega \sin\psi_0 (x\cos\theta_0 + y\sin\theta_0) + i\Omega z\cos\psi_0\right], \tag{2.6a}$$

$$(\phi_0 + \phi)'\big|_{y=0} = -i\Omega^2\left[(1-\alpha_H)\eta + \alpha_H \eta_a\right], \tag{2.6b}$$

$$(1-\alpha_H)\left\{\nabla_{x,z}^4 - 1\right\}\eta = \frac{\epsilon}{\Omega^5}\left(1 + \alpha_H \bar{K}_R\right)\Delta p, \tag{2.6c}$$

$$\Delta p = -\mathrm{i}\Omega^2 D(x), \qquad (2.6d)$$

$$\left(\nabla^2_{x,y} + k^2\right)\phi = 0, \qquad (2.6e)$$

where the prime denotes the operation $\partial/\partial y$. Note that the parameter group $\bar{K}_R = 2K_R/(\pi R)$ and function $D(x) = \phi(x, 0^+, z) - \phi(x, 0^-, z)$ have been defined for convenience, and the amplitude of the incident wave has been chosen such that it has unit strength. These equations suggest that $\exp[\mathrm{i}\Omega(r_0 + z\cos\psi_0)]/r_0$ is common to the entire field, which allows this term and the variations in the z-direction to be suppressed until the end of the analysis.

3. The Wiener–Hopf equation

Now define the Fourier half-range transforms by

$$\Phi(\alpha, y) = \int_{-\infty}^{0} \phi(x, y)\mathrm{e}^{\mathrm{i}\alpha x}\,\mathrm{d}x + \int_{0}^{\infty} \phi(x, y)\mathrm{e}^{\mathrm{i}\alpha x}\,\mathrm{d}x,$$
$$= \Phi_-(\alpha, y) + \Phi_+(\alpha, y), \qquad (3.1)$$

where $\alpha = \sigma + \mathrm{i}\tau$ is the complex transform variable. These 'plus' and 'minus' functions are regular in the upper and lower complex planes defined by R_+ and R_-, respectively, which are to be set as the Wiener–Hopf equation is derived. Note that the introduction of a small dissipation term in the frequency allows the reduced wavenumber to be written as $k = k_1 + \mathrm{i}k_2$, where $k_1, k_2 > 0$.

The solution to the transformed Helmholtz equation is found by enforcing boundedness at $y \to \pm\infty$, and by observing that the velocity normal to the x–z plane, $\Phi'(\alpha, 0)$, is continuous for all x, so that

$$\Phi(\alpha, y) = \mathrm{sgn}(y)A(\alpha)\mathrm{e}^{-\gamma|y|}. \qquad (3.2)$$

Here $\gamma = \sqrt{\alpha^2 - k^2}$ is defined with branch cuts joining the points $\pm k$ to infinity through the upper and lower half-planes and such that γ tends to α as $\alpha \to \infty$ along the positive real axis. From this solution we can write

$$\Phi(\alpha, 0^+) - \Phi(\alpha, 0^-) = 2A(\alpha) = D_-(\alpha), \qquad (3.3)$$

$$\Phi'(\alpha, 0) \equiv \Phi'_-(\alpha, 0) + \Phi'_+(\alpha, 0) = -\gamma A(\alpha), \qquad (3.4)$$

where the final step in (3.3) follows from the fact that Φ is continuous across $y = 0$ for $x > 0$.

Taking the Fourier transform of the kinematic boundary condition (2.6b) between the fluid and the poroelastic plate yields

$$-\mathrm{i}\Omega^2(1 - \alpha_H)H_-(\alpha) = \Phi'_-(\alpha, 0) - \alpha_H\left(\frac{\bar{K}_R}{2R}\right)D_-(\alpha) - \frac{k\sin\theta_0}{\alpha - k\cos\theta_0}, \qquad (3.5)$$

where $H_-(\alpha)$ is the half-transform of the plate deflection, η. Next, transforming the poroelastic-plate equation (2.6c) and multiplying by $-\mathrm{i}\Omega^2$, we find

$$(1 - \alpha_H)\left\{\left[\alpha^2 - (k^2 - \Omega^2)\right]^2 - 1\right\}H_-(\alpha)$$

$$+ \frac{\mathrm{i}\epsilon}{\Omega^3}\left(1 + \alpha_H\bar{K}_R\right)D_-(\alpha) + (1 - \alpha_H)h(\alpha) = 0, \qquad (3.6)$$

where

$$h(\alpha) = \frac{\partial^3 \eta(0)}{\partial x^3} - i\alpha \frac{\partial^2 \eta(0)}{\partial x^2} - \left[\alpha^2 - 2(k^2 - \Omega^2)\right] \left[\frac{\partial \eta(0)}{\partial x} - i\alpha \eta(0)\right]. \quad (3.7)$$

The term $h(\alpha)$ contains four plate edge conditions at $x = 0$, only two of which may be prescribed. The other two must be determined as part of the solution.

Substituting (3.6) into (3.5) and eliminating $\Phi'_-(\alpha, 0) = -\gamma D_-(\alpha)/2 - \Phi'_+(\alpha, 0)$, we arrive at a scalar Wiener–Hopf equation

$$\frac{1}{2} K(\alpha) D_-(\alpha) + \Phi'_+(\alpha, 0) = -\frac{k \sin \theta_0}{\alpha - k \cos \theta_0}$$

$$- \frac{i\Omega^2 (1 - \alpha_H) h(\alpha)}{\left[\alpha^2 - (k^2 - \Omega^2 - 1)\right] \left[\alpha^2 - (k^2 - \Omega^2 + 1)\right]}, \quad (3.8)$$

where the kernel $K(\alpha)$ is defined by

$$K(\alpha) = (\alpha^2 - k^2)^{1/2} + \frac{\alpha_H \bar{K}_R}{R} - \frac{\epsilon}{\Omega} \frac{1 + \alpha_H \bar{K}_R}{\left[\alpha^2 - (k^2 - \Omega^2 - 1)\right] \left[\alpha^2 - (k^2 - \Omega^2 + 1)\right]}. \quad (3.9)$$

The Wiener–Hopf equation contains on the left-hand side unknown functions that are regular in regions of the complex plane R_+ or R_-, and functions on the right-hand side regular in the strip of overlap S between R_+ and R_-. The branch cut definition for $\gamma(\alpha)$ and convergence requirement for the transform integral of (2.6b) demand that $R_+(\tau > -k_2)$ and $R_-(\tau < k_2 \cos \theta_0)$, respectively. Further restrictions on the definition of strip S come from the migration behaviour of the poles in $K(\alpha)$ as $k_2 \searrow 0$ in the sense of the Briggs–Bers stability criterion (Briggs 1964; Bers 1983). This procedure leads to the additional conditions:

$$\left\{\tau > \text{Im}(\sqrt{k^2 - \Omega^2 - 1}), \tau > \text{Im}(-\sqrt{k^2 - \Omega^2 + 1})\right\} \quad \text{in } R_+, \quad (3.10)$$

$$\left\{\tau < \text{Im}(-\sqrt{k^2 - \Omega^2 - 1}), \tau < \text{Im}(\sqrt{k^2 - \Omega^2 + 1})\right\} \quad \text{in } R_-, \quad (3.11)$$

for the parameter range $\Omega^2 \cos^2 \psi_0 < 1/2$, which includes the parameter regime of interest to the owl noise problem. Defining $\alpha_1 \equiv \sqrt{k^2 - \Omega^2 - 1}$ and $\alpha_2 \equiv \sqrt{k^2 - \Omega^2 + 1}$, the strip of overlap S, $\tau_- < \tau < \tau_+$, between the regions of regularity in the upper and lower complex planes may be stated as

$$S \in \max\{-k_2, \text{Im}(\alpha_1), \text{Im}(-\alpha_2)\} < \text{Im}(\alpha) < \min\{k_2 \cos \theta_0, \text{Im}(-\alpha_1), \text{Im}(\alpha_2)\}. \quad (3.12)$$

4. Solution of the scattered field

The Wiener–Hopf equation must now be factorized into functions regular in either R_- or R_+. Because the kernel $K(\alpha)$ has no zeros in the strip S, it may be written as $K(\alpha) \equiv K_-(\alpha) K_+(\alpha)$, where this multiplicative factorization will be carried out numerically. Let the right-hand side of (3.8) divided by $K_+(\alpha)$ be defined as $L(\alpha) = L_1(\alpha) + L_2(\alpha)$, where $L_1(\alpha) = -k \sin \theta_0 / [K_+(\alpha)(\alpha - k \cos \theta_0)]$. The additive factorizations of $L_1(\alpha)$ and $L_2(\alpha)$ are accomplished in the usual fashion via the Cauchy integral theorem (Noble 1988, p. 13), where the 'minus' functions are evaluated first, and then $L_+(\alpha) = L(\alpha) - L_-(\alpha)$. Thus, it is sufficient to note the following results of

the additive factorization:

$$L_{1-}(\alpha) = -\frac{k \sin \theta_0}{K_+(k \cos \theta_0)(\alpha - k \cos \theta_0)}, \tag{4.1}$$

$$L_{2-}(\alpha) = -\frac{1}{4}i\Omega^2(1 - \alpha_H)\left\{\frac{h(-\alpha_1)}{\alpha_1 K_+(-\alpha_1)(\alpha + \alpha_1)} + \frac{h(\alpha_2)}{\alpha_2 K_+(\alpha_2)(\alpha - \alpha_2)}\right\}. \tag{4.2}$$

The Wiener–Hopf equation (3.8) can now be separated into 'minus' and 'plus' functions on the left and right sides, respectively, which are both equal to an entire function $E(\alpha)$ in the strip S:

$$\frac{1}{2}K_-(\alpha)D_-(\alpha) - L_-(\alpha) = L_+(\alpha) - \frac{\Phi'_+(\alpha, 0)}{K_+(\alpha)}, \tag{4.3}$$

$$= E(\alpha). \tag{4.4}$$

By appeal to the extended Liouville theorem, $E(\alpha)$ must be a polynomial in α provided that it can be shown that both sides of (4.3) have only algebraic growth as $|\alpha| \to \infty$. The multiplicative kernel may be written as $K(\alpha) = (\alpha - k)^{1/2}(\alpha + k)^{1/2}J(\alpha)$, where $(\alpha \mp k)^{1/2}$ are regular in the lower/upper complex half-planes and $J(\alpha) \to 1$ as $|\alpha| \to \infty$. Thus, $K_\pm(\alpha) \sim |\alpha|^{1/2}$ as $|\alpha| \to \infty$. The behaviour of $L_\pm(\alpha) \sim O(|\alpha|^{-1})$ may be found by inspection, noting that the terms in $L_+(\alpha)$ involving the edge conditions decay faster than $|\alpha|^{-1}$ as $|\alpha| \to \infty$ regardless of the boundary conditions at the edge.

The behaviour of $\Phi'_+(\alpha, 0)$ and $D_-(\alpha)$ at large $|\alpha|$ may be found using the Abel theorem (Crighton & Leppington 1970; Noble 1988). We anticipate the usual edge behaviour $\partial \phi/\partial y|_{y=0} \sim x^{-1/2}$ as $x \to 0^+$ in the absence of a mean flow. (However, we note that the following results from the Abel theorem also hold for the mathematically weaker edge condition $\partial \phi/\partial y|_{y=0} \sim x^0$ if a Kutta condition imposes a finite velocity at the edge when a mean flow exists in the positive x-direction.) Applying the Abel theorem,

$$\Phi'_+(\alpha, 0) \sim \int_0^\infty \phi'(x \to 0^+, 0)e^{i\alpha x}\,dx \sim |\alpha|^{-1/2} \tag{4.5}$$

as $|\alpha| \to \infty$ with $\tau > \tau_-$. Similarly, we note that $D(x)$ is a continuous function that is identically zero for $x > 0$, which allows us to write $D(x) \sim (-x)^\xi$ as $x \to 0^-$, $\xi > 0$, so that

$$D_-(\alpha) \sim \int_{-\infty}^0 (-x)^\xi\,e^{i\alpha x}\,dx \sim |\alpha|^{-\xi-1} \tag{4.6}$$

as $|\alpha| \to \infty$ with $\tau < \tau_+$. Therefore, $K_-(\alpha)D_-(\alpha) \sim |\alpha|^{-\xi-1/2}$ and $\Phi'_+(\alpha, 0)/K_+(\alpha) \sim |\alpha|^{-1}$, and the terms on each side of (4.3) decay as $|\alpha|^{-1/2}$ or faster as $|\alpha| \to \infty$. Thus, the entire function is identically zero, $E(\alpha) \equiv 0$, and the Wiener–Hopf equation provides two equations for the unknown functions $D_-(\alpha)$ and $\Phi'_+(\alpha, 0)$, i.e.

$$D_-(\alpha) = \frac{2L_-(\alpha)}{K_-(\alpha)}, \tag{4.7}$$

$$\Phi'_+(\alpha, 0) = K_+(\alpha)L_+(\alpha). \tag{4.8}$$

Recall that the transformed poroelastic-plate equation produced four end conditions at $x = 0$ that are contained in $h(\alpha)$ (see (3.7)). We now specify the free-edge plate

boundary conditions (Timoshenko 1940; Rayleigh 1945) at $x = 0$ relevant to the trailing-edge noise problem. Recalling that $\partial/\partial z = \mathrm{i}k_0 \cos \psi_0$, the free-edge boundary conditions are:

$$\frac{\partial^3 \eta(0)}{\partial x^3} + (2 - \nu)(k^2 - \Omega^2) \frac{\partial \eta(0)}{\partial x} = 0, \tag{4.9}$$

$$\frac{\partial^2 \eta(0)}{\partial x^2} + \nu(k^2 - \Omega^2)\eta(0) = 0. \tag{4.10}$$

To identify the two remaining equations necessary to fully determine the edge conditions required in (3.7), we substitute (4.7) and (4.8) into (3.5), and using the fact that $\Phi'_+(\alpha, 0) = -\gamma(\alpha)D_-(\alpha)/2 - \Phi'_-(\alpha, 0)$ find

$$\mathrm{i}\Omega^2(1 - \alpha_H)H_-(\alpha) = \left[\gamma(\alpha) + \frac{\alpha_H \bar{K}_R}{R}\right] \frac{L_-(\alpha)}{K_-(\alpha)} + K_+(\alpha)L_+(\alpha) + \frac{k \sin \theta_0}{\alpha - k \cos \theta_0}. \tag{4.11}$$

The half-transform of the plate deflection, $H_-(\alpha)$, is regular in R_- by definition, a condition which is apparently violated in (4.11) by the poles in the lower complex half-plane contained in $K_+(\alpha)L_+(\alpha)$. Therefore, the two additional equations to determine the edge conditions arise from the mathematical requirement that the poles of $K_+(\alpha)L_+(\alpha)$ in R_- lead to merely removable singularities in $H_-(\alpha)$. To make the influence of these poles explicit, we reorganize the kernel $K(\alpha)$ into the form

$$K(\alpha) = \underbrace{\frac{I_+(\alpha)}{(\alpha - \alpha_1)(\alpha + \alpha_2)}}_{K_+(\alpha)} \underbrace{\frac{I_-(\alpha)}{(\alpha + \alpha_1)(\alpha - \alpha_2)}}_{K_-(\alpha)}, \tag{4.12}$$

where

$$I(\alpha) = \left\{\gamma(\alpha) + \frac{\alpha_H \bar{K}_R}{R}\right\}(\alpha^2 - \alpha_1^2)(\alpha^2 - \alpha_2^2) - \frac{\epsilon}{\Omega}(1 + \alpha_H \bar{K}_R). \tag{4.13}$$

The requirement that the singularities at $\alpha = \alpha_1$ and $\alpha = -\alpha_2$ are removable in (4.11) furnishes two linear expressions that complete the system of equations. The coefficients of these expressions and the details of the numerical kernel splitting procedure are given in appendix A.

With the edge conditions in $h(\alpha)$ now fully determined, we proceed with the solution of the scattered field from (4.8). The Abel theorem may be employed again to determine the scattered field very close to the edge due to the incident plane wave from the far field, which by the reciprocal theorem produces the far-field acoustic solution due to a source near the poroelastic edge. Following the arguments by Crighton & Leppington (1970), the field for points close to the edge ($|\boldsymbol{x}| \to 0$, strictly speaking) may be evaluated from the asymptotic limit of the Wiener–Hopf solution as $|\alpha| \to \infty$, i.e.

$$\Phi'_+(\alpha, 0) = -\mathrm{i}\Omega^2(1 - \alpha_H) \left\{ \frac{h(\alpha)}{(\alpha^2 - \alpha_1^2)(\alpha^2 - \alpha_2^2)} - \frac{1}{4}K_+(\alpha) \left[\frac{h(-\alpha_1)}{\alpha_1 K_+(-\alpha_1)(\alpha + \alpha_1)} \right. \right.$$

$$\left. \left. + \frac{h(\alpha_2)}{\alpha_2 K_+(\alpha_2)(\alpha - \alpha_2)} \right] \right\} - \frac{k \sin \theta_0}{\alpha - k \cos \theta_0} \left[1 - \frac{K_+(\alpha)}{K_+(k \cos \theta_0)} \right], \tag{4.14}$$

$$\sim B\alpha^{-1/2} \quad \text{as } |\alpha| \to \infty, \tag{4.15}$$

where

$$B \equiv \frac{1}{4}\mathrm{i}\Omega^2(1-\alpha_H)\left[\frac{h(-\alpha_1)}{\alpha_1 K_+(-\alpha_1)} + \frac{h(\alpha_2)}{\alpha_2 K_+(\alpha_2)}\right] + \frac{k\sin\theta_0}{K_+(k\cos\theta_0)}. \tag{4.16}$$

The Abel theorem (Noble 1988, p. 36) provides the following condition on the scattered field:

$$\frac{\partial\phi}{\partial y}(x\to 0^+,0) \propto (\pi x)^{-1/2}. \tag{4.17}$$

The fact that $\phi(x,y)$ is odd and continuous in y about $y=0$ when $x>0$ provides a second condition for the scattered field,

$$\frac{\partial\phi}{\partial x}(x,0)=0 \quad \text{for } x>0. \tag{4.18}$$

Recalling (2.4), it is clear that the flow near the plate edge is incompressible (Crighton & Leppington 1970), and the edge condition (4.17) indicates that the near-field solution has the form (Batchelor 1967, p. 410)

$$\phi(\bar{r},\theta) = C_1\bar{r}^{1/2}\cos\frac{\theta}{2} + C_2\bar{r}^{1/2}\sin\frac{\theta}{2} \quad \text{as } \bar{r}\to 0, \tag{4.19}$$

where $\bar{r}=r\sin\psi$, $x=\bar{r}\cos\theta$ and $y=\bar{r}\sin\theta$. The application of (4.17) and (4.18) to (4.19) yields the near-field solution for the scattered field,

$$\phi = -2\mathrm{i}\,\bar{r}^{1/2}\pi^{-1/2}B\sin\frac{\theta}{2}\frac{\exp\left[\mathrm{i}(\Omega r_0 + \Omega z\cos\psi_0 + \pi/4)\right]}{r_0} \quad \text{as } \bar{r}\to 0. \tag{4.20}$$

At this point the source and observer may be exchanged by asserting reciprocity (Rayleigh 1945, §294), where ϕ can now be regarded as the scattered solution measured in the acoustic far field due to a source located close to the edge at coordinates (r_0,θ_0,ψ_0).

The dominant scattered quadrupole field has axes aligned with the x and y directions (Crighton & Leppington 1970),

$$\frac{\partial^2\phi}{\partial x\partial y} = \frac{\mathrm{i}B\cos\frac{3\theta}{2}}{2\sqrt{\pi}\,\bar{r}^{3/2}}\frac{\exp\left[\mathrm{i}(\Omega r_0 + \Omega z\cos\psi_0 + \pi/4)\right]}{r_0}, \tag{4.21}$$

which is to be compared with the quadrupole strength of the incident field,

$$\frac{\partial^2\phi_0}{\partial x\partial y} = -\Omega^2\sin^2\psi_0\cos\theta_0\sin\theta_0\frac{\exp\left[\mathrm{i}(\Omega r_0 + \Omega z\cos\psi_0)\right]}{r_0}. \tag{4.22}$$

An amplification factor β can now be defined as the ratio of the strength of the scattered field to that of a quadrupole source near the poroelastic edge. Neglecting directivity and other $O(1)$ terms, the amplification factor becomes

$$\beta \sim \frac{|B|}{\Omega^2\bar{r}^{3/2}}, \tag{4.23}$$

where B, as defined by (4.16), depends on Ω, the properties of the poroelastic edge, and the directivity of the incident field. In general, the dependence of B on these parameters must be determined numerically. However, progress can be made analytically when considering the porous and elastic effects separately and constructing

certain asymptotic factorizations of the associated simpler Wiener–Hopf kernels. This approach identifies the appropriate parametric limits to anticipate the scaling behaviour of the numerical solutions with respect to frequency, flow velocity, and intrinsic fluid loading and will be described in the next section.

5. Asymptotic results for the aerodynamic noise problem

The amplification factor (4.23) will now be linked to the acoustic power observed in the far field due to a turbulent eddy near the poroelastic edge. Following the arguments of Crighton & Leppington (1970), we suppose that the turbulence is characterized by a root-mean-squared velocity u_0 and an integral correlation length l_0, parameters which are non-dimensionalized in the same manner as in (2.5). Thus, the associated frequency of the turbulent eddy is u_0/l_0. Provided that the Mach number $M = u_0/c_0$ is sufficiently small, the frequency of the eddy will be the same as that of the emitted radiation, resulting in an acoustic wavenumber $\Omega = Ml_0^{-1}$. The acoustic power emitted to the far field is proportional to the square of the pressure, which is proportional to the velocity potential of the scattered field. Therefore, the acoustic power due to the half-plane scattering relative to the acoustic power of a free-field quadrupole is $\Pi/\Pi_0 \sim \beta^2$, and employing the celebrated 'eighth power' law (Lighthill 1952) for Π_0, we find

$$\Pi \sim \beta^2 u_0^3 M^5. \tag{5.1}$$

Also, the velocity dependence contained within the amplification factor β is strictly due to its dependence on frequency, Ω. Therefore, the Ω-exponent of β^2 contributes to the velocity scaling of Π.

5.1. *Impermeable rigid edge*

The special case of a rigid and non-porous edge permits an exact analytical solution that furnishes a check on the numerical kernel splitting procedure for $\alpha_H = 0$ and $\epsilon = 0$. In this case, $K(\alpha) = (\alpha^2 - k^2)^{1/2}$, and the necessary factorization is achieved on sight. The essential results are:

$$B_r = \frac{k\sin\theta_0}{K_+(k\cos\theta_0)} = (2\Omega)^{1/2}\sin\frac{\theta_0}{2}\sin^{1/2}\psi_0 \sim \Omega^{1/2}, \tag{5.2}$$

$$\left(\frac{\partial^2\phi}{\partial x\partial y}\right)_r = \frac{i\Omega^{1/2}\sin\dfrac{\theta_0}{2}\sin^{1/2}\psi_0\cos\dfrac{3\theta}{2}}{\sqrt{2\pi}\bar{r}^{3/2}}\frac{\exp\left[i(\Omega r_0 + \Omega z\cos\psi_0 + \pi/4)\right]}{r_0}, \tag{5.3}$$

$$\beta_r \sim (\Omega\bar{r})^{-3/2}, \tag{5.4}$$

$$\Pi_r \sim u_0^3 M^2 \sim u_0^5, \tag{5.5}$$

which agree with the work of Ffowcs Williams & Hall (1970) and Crighton & Leppington (1970). In particular, the famous u_0^5 scaling of the far-field acoustic power is recovered in this limit.

5.2. *Porous rigid edge*

The introduction of porosity to a rigid edge modifies (3.9) to take the form

$$K(\alpha) = (\alpha^2 - k^2)^{1/2} + \mu, \tag{5.6}$$

where the porous effects are embodied by a single parameter, $\mu = \alpha_H \bar{K}_R/R$. The kernel (5.6) takes the well-known Kranzer–Radlow form (Kranzer & Radlow 1962, 1965;

Kranzer 1968) that permits asymptotic evaluations of $K_+(k\cos\theta_0)$ when $\delta = \mu/k \ll 1$ or $\delta \gg 1$. As noted by Leppington (1977), the modelling of porosity as a Rayleigh conductivity boundary condition leads to the same Wiener–Hopf kernel as an equivalent point-reacting compliant edge. The asymptotic results of Crighton & Leppington (1970) for this type of kernel are exploited below for the present porous rigid edge configuration.

After a simple rescaling, the kernel (5.6) can be written as

$$K(\alpha, \delta) = K^{(0)}(\alpha) + \delta K^{(1)}(\alpha). \tag{5.7}$$

For $\delta \ll 1$, Noble (1988, pp. 160–164) discusses how multiplicative factors for kernels of this form can be described by

$$K_\pm(\alpha, \delta) = K_\pm^{(0)}(\alpha) + \delta K_\pm^{(1)}(\alpha) + o(\delta), \tag{5.8}$$

and Crighton & Leppington (1970) show that this solution procedure leads to

$$K_\pm(\alpha, \delta) = (\alpha \pm k)^{1/2} \left\{ 1 + \frac{\delta}{\pi (\alpha^2 - k^2)^{1/2}} \arccos\left(\pm\frac{\alpha}{k}\right) + o(\delta) \right\}, \tag{5.9}$$

where $\arccos z = i \ln(z + \sqrt{z^2 - 1})$. Equation (5.9) is simply a first-order correction to the factored rigid impermeable kernel to account for the effects of porosity. Therefore, the leading-order behaviour of the rigid porous edge in the limit $\delta \ll 1$ is the same as if the edge were impermeable.

The value of $K_+(k\cos\theta_0)$ in the opposite limit $\delta \gg 1$ was derived by Crighton & Leppington (1970) by constructing an exact factorization and determining the appropriate leading-order term. Crighton (2001) attacks (5.6) in this limit using a novel application of matched asymptotic expansions, and the result from both approaches is

$$K_+(k\cos\theta_0) \sim \mu^{1/2} e^{i\pi/4} \quad \text{for } \delta \gg 1. \tag{5.10}$$

The B term (4.16) in the amplification factor for a rigid edge, whether porous or not, is $k\sin\theta_0/K_+(k\cos\theta_0)$. Therefore, the following scaling estimates of the amplification factor are made for the two limits of low and high effective porosity, respectively:

$$\beta_{rp} \sim \begin{cases} \Omega^{-3/2}, & \delta \ll 1 \\ (\alpha_H/R)^{-1/2} \Omega^{-1}, & \delta \gg 1. \end{cases} \tag{5.11}$$

The acoustic power scaling for scattered sound in the far field follows immediately from (5.11), as

$$\Pi_{rp} \sim \begin{cases} u_0^3 M^2, & \alpha_H \bar{K}_R/(kR) \ll 1 \\ (\alpha_H/R)^{-1} u_0^3 M^3, & \alpha_H \bar{K}_R/(kR) \gg 1, \end{cases} \tag{5.12}$$

respectively.

Ffowcs Williams (1972) arrives at the same U^6 scaling in the high-porosity limit in a theoretical study of turbulence interacting with an infinite perforated surface; subsequent experiments by Nelson (1982) corroborate this dipole-like velocity scaling. Surprisingly, the U^6 behaviour also holds for the present semi-infinite geometry when $\delta = \alpha_H \bar{K}_R/(kR) \gg 1$, indicating that the effect of the edge on the scattered sound is eliminated in this limit. However, the presence of the edge becomes important in the low-porosity limit where the U^5 scaling is recovered, as it would for an equivalent point-reacting compliant edge (Crighton & Leppington 1970), whereas

an infinite porous surface would support an altogether different monopole-type U^4 behaviour (Ffowcs Williams 1972).

5.3. *Elastic edge*

Now consider the special case of turbulence scattered by an impermeable elastic edge ($\alpha_H = 0$). Setting the small parameter to be $\kappa_1 = \Omega^{-1}\epsilon \ll 1$, the Wiener–Hopf kernel (3.9) takes the form:

$$K(\alpha, \kappa_1) = (\alpha^2 - k^2)^{1/2} - \kappa_1 (\alpha^2 - \alpha_1^2)^{-1} (\alpha^2 - \alpha_2^2)^{-1}. \qquad (5.13)$$

This kernel is a modest extension of the so-called 'perturbed kernel' analysed previously for the porous and rigid edge, where now the small parameter κ_1 multiplies an integral function that can be factorized on sight. The solution procedure outlined in appendix B produces a first-order correction to the rigid impermeable results to account for elastic effects,

$$K_+(\alpha, \kappa_1) = (\alpha + k)^{1/2}(1 - \kappa_1 F_+(\alpha) + o(\kappa_1)). \qquad (5.14)$$

Trial and error reveals a second scaling parameter of the elastic kernel: $\kappa_2 = \Omega\epsilon^{-1/2}$. The asymptotic evaluation of $K_+(k\cos\theta_0)$ will be treated as solving for $K_+(\lambda = O(1))$, where $\lambda = \alpha/\Omega$, using the matched asymptotic expansion procedure developed by Crighton (2001). We are concerned first with the inner scaling and proceed by determining $K(\lambda, \kappa_2)$ when $\lambda = O(1)$ as $\kappa_2 \to 0$, namely

$$K(\lambda, \kappa_2) \sim \Omega\kappa_2^{-2} \left\{ 1 + \kappa_2^2 (\lambda^2 - \sin^2\psi_0)^{1/2} \right\}. \qquad (5.15)$$

Further changes of variables $\delta = \kappa_2^2$, $\chi = \delta \sin\psi_0$, $\bar{\lambda} = \lambda \operatorname{cosec} \psi_0$ lead to

$$K(\bar{\lambda}, \chi) \sim \Omega\delta^{-1} \left\{ 1 + \chi (\bar{\lambda}^2 - 1)^{1/2} \right\}, \qquad (5.16)$$

$$= \Omega\delta^{-1} Q(\bar{\lambda}, \chi). \qquad (5.17)$$

Thus, a Kranzer–Radlow-type kernel $Q(\bar{\lambda}, \chi)$ appears in the same form as the high-porosity limit for the porous rigid edge. In this situation, Crighton (2001) shows that $Q_+ \sim a_0$, some complex constant, for the inner expansion when $\bar{\lambda} = O(1)$. The outer expansion yields a behaviour $Q_+ \sim \zeta^{1/2}$ for $\zeta = \chi\bar{\lambda} \to \infty$. We require in the original kernel that $K_+(\alpha) \sim |\alpha|^{1/2}$ as $|\alpha| \to \infty$, which is readily shown when the necessary substitutions are made, and the constant a_0 is determined by matching the inner and outer expansions of the kernel factor in the appropriate Van Dyke sense (Crighton & Leppington 1973; Van Dyke 1975). Dropping $O(1)$ constants that are of no consequence to the scaling behaviour of the kernel factors, the essential results for both asymptotic limits for the elastic edge are:

$$K_+(k\cos\theta_0) \sim \Omega^{-1/2}\epsilon^{1/2} \quad \text{for } \kappa_2 = \Omega\epsilon^{-1/2} \ll 1, \qquad (5.18)$$

$$K_+(k\cos\theta_0) \sim \Omega^{1/2} \quad \text{for } \kappa_1^{-1} = \Omega\epsilon^{-1} \gg 1. \qquad (5.19)$$

The numerical evaluation of $K_+(k\cos\theta_0)$ in figure 2 confirms these scaling results, where the transition between the high and low limits is best described by the parametric group $\Omega\epsilon^{-1/2}$. The directivity of the incident field is herein set to $\psi_0 = \pi/2$ and $\theta_0 = \pi/4$ to focus on the dependence of the acoustic amplification on the edge properties.

In contrast to the rigid edge cases, the elastic edge requires the solution of a linear system of equations (4.9), (4.10), (A 1) and (A 2) involving the edge conditions
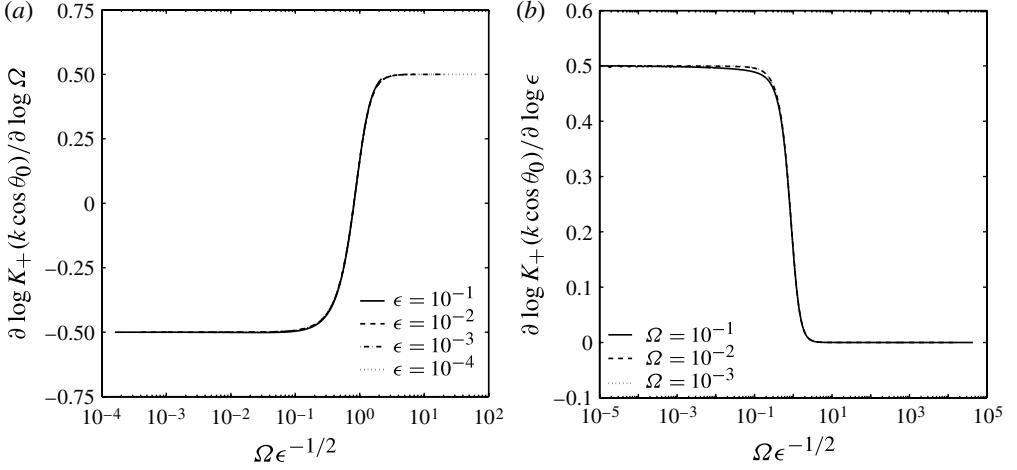
FIGURE 2. Scaling exponents of $K_+(k\cos\theta_0)$ for an elastic edge: (*a*) exponent of Ω; (*b*) exponent of ϵ.

to proceed to an order-of-magnitude estimate for the sound amplification factor, β. Noting the simplifications of α_1 and α_2 when $\Omega^2 \ll 1$, a heuristic magnitude estimate of (4.16) leads with (4.23) to

$$\beta_e \sim \frac{1}{\Omega K_+(k\cos\theta_0)}. \tag{5.20}$$

For small Ω in the sense that $\Omega\epsilon^{-1/2} \ll 1$, direct substitution of (5.18) yields the scaling estimate

$$\beta_e \sim \Omega^{-1/2}\epsilon^{-1/2}. \tag{5.21}$$

Figure 3 confirms the elastic scattering amplification $\beta_e \sim \epsilon^{-1/2}$ in this small-Ω limit, and that in the upper limit the intrinsic fluid loading parameter has no effect. The numerical solutions indicate a transition from $\beta_e \sim \epsilon^{-1/2}$ to $\beta_e \sim \epsilon^0$ that depends on both $\Omega\epsilon^{-1}$ and $\Omega\epsilon^{-1/2}$.

A more complicated picture emerges in figure 4 for the dependence of the scattered field on the frequency parameter Ω, where the amplification factor collapses across three distinct parameter scalings. Of particular interest is the existence of a region $\beta \sim \Omega^{-1/2}$, predicted by the result (5.21), for the approximate finite range $0.1\epsilon < \Omega < 0.1\epsilon^{1/2}$ as determined from figure 4(*a*,*b*). Figure 3 indicates that within this range the amplification dependence on ϵ varies, but the fixed scaling for Ω furnishes a U^7 velocity dependence for the far-field acoustic power,

$$\Pi_e \sim u_0^3 M^4 \quad \text{for } \epsilon < 10\Omega < \epsilon^{1/2}. \tag{5.22}$$

Clearly, the heuristic arguments to arrive at (5.22) do not hold for $\Omega\epsilon^{-1} \ll 1$ as shown in figure 4(*a*). A more rigorous approach to determine additional scaling information analytically would seek to construct a uniformly valid composite expression for $\beta_e = \beta_e(\Omega, \epsilon)$ using the Van Dyke (1975) matching principle across regions described by Ω, $\Omega\epsilon^{-1/2}$ and $\Omega\epsilon^{-1}$. However, the need to evaluate the edge conditions for $h(\alpha)$ in (3.7) complicates this course of action, and it will not be pursued further here.
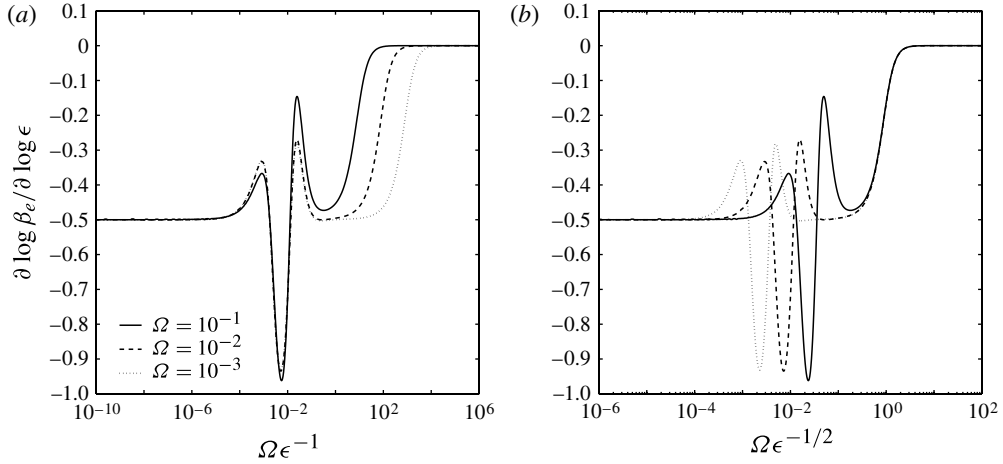
FIGURE 3. Exponent of ϵ for the elastic-edge amplification factor β_e as a function of rescaled wavenumber: (*a*) exponent as a function of $\Omega\epsilon^{-1}$; (*b*) exponent as a function of $\Omega\epsilon^{-1/2}$.
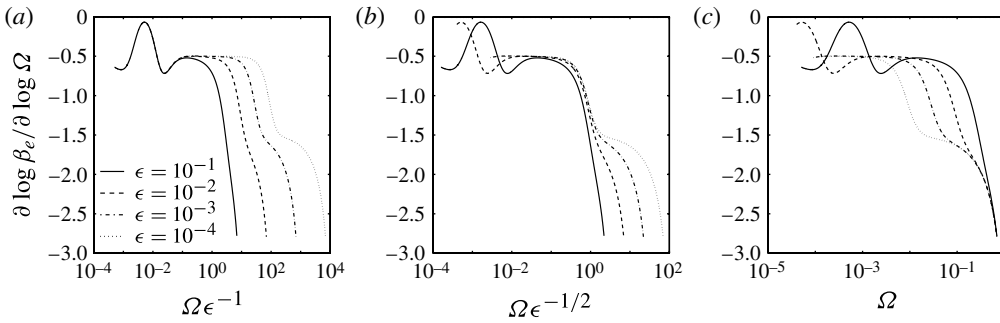

FIGURE 4. Exponent of Ω for the elastic-edge amplification factor as a function of rescaled wavenumber for several values of ϵ: (*a*) exponent as a function of $\Omega\epsilon^{-1}$; (*b*) exponent as a function of $\Omega\epsilon^{-1/2}$; (*c*) exponent as a function of Ω.

6. Numerical results for a poroelastic edge

We now choose a baseline set of parameters based upon the experiments by Herr (2007), which examine the reduction of trailing-edge noise using a flexible polypropylene brush. Handbook values for the elastic modulus and density of polypropylene, $E \approx 2$ GPa and $\rho \approx 900$ kg m^{-3}, respectively, match closely with the properties of feather keratin that comprises the owl trailing-edge fringe. Bonser & Purslow (1995) cite an elastic modulus range of 1.78–2.5 GPa, and the density of keratin found in chicken feathers, for example, was found to be 890 kg m^{-3} as measured by Barone & Schmidt (2005). The Poisson ratio plays a minor role in the present analysis, and its value is set to $\nu = 0.3$, which is representative of many common materials. The flexible brush geometry is physically different from the poroelastic-plate model with evenly spaced circular holes that is considered in the present work; however, a set of parameters may be roughly approximated using the hydraulic diameter of the region between the fibres, a metric which is dominated by the spacing between the fibres. Here we take the fibre geometry for the best noise-reduction case by Herr (2007), where the fibre diameter, length, and spacing
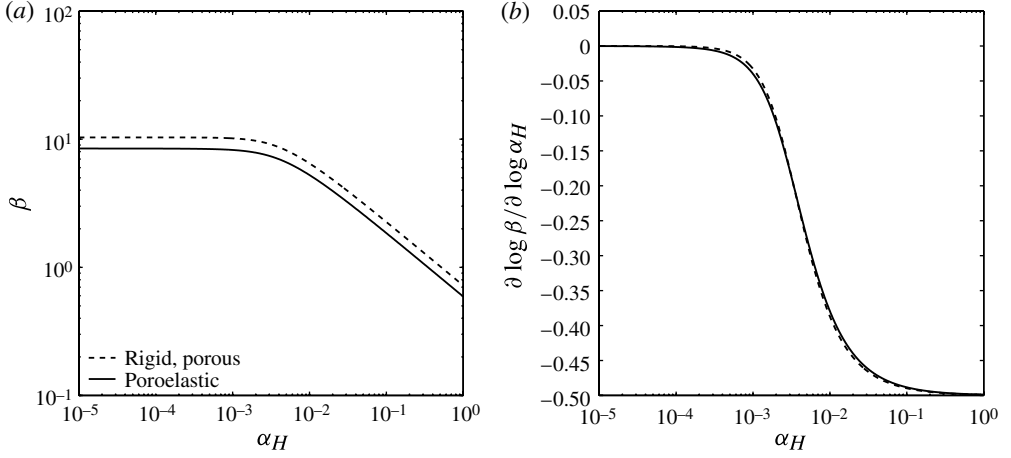
FIGURE 5. Dependence of quadrupole edge noise amplification on the fractional open area: (*a*) logarithmic variation; (*b*) slope of logarithmic plot. $\Omega = 0.14$, $R = 0.026$; $\epsilon = 0.002$ for the poroelastic case.
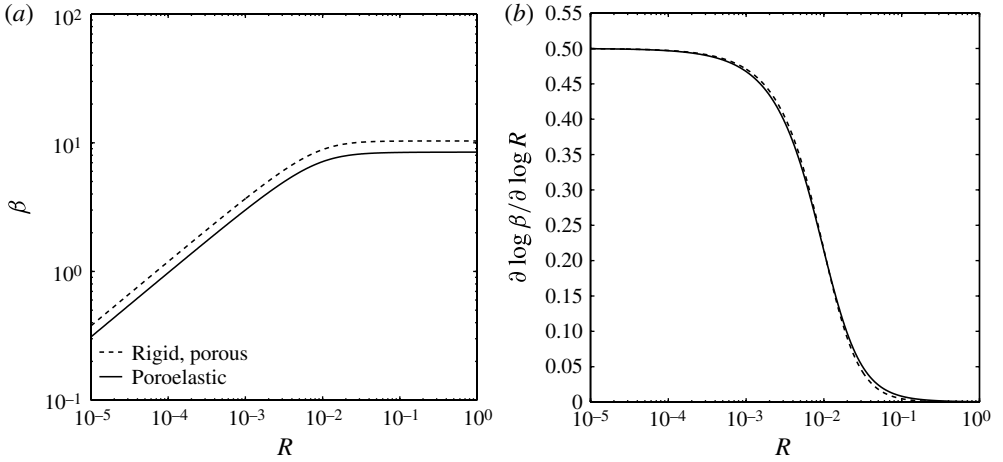

FIGURE 6. Dependence of quadrupole edge noise amplification on the non-dimensional aperture radius: (*a*) logarithmic variation; (*b*) slope of logarithmic plot. $\Omega = 0.14$, $\alpha_H = 0.0014$; $\epsilon = 0.002$ for the poroelastic case.

along the trailing edge are 0.4, 45 and $\leqslant 0.1$ mm, respectively. Supposing a turbulent eddy near the poroelastic edge with a characteristic frequency of 2 kHz, the baseline dimensionless parameters for the numerical simulations are: $\alpha_H = 0.0014$, $R = 0.026$, $\epsilon = 0.002$ and $\Omega = 0.14$.

The turbulent noise amplification predicted by the full poroelastic model is compared in figures 5 and 6 against the special case of a rigid porous edge in terms of the fractional open area α_H and the pore radius non-dimensionalized by the bending wavelength R. The differences in the amplification factor and associated scaling behaviours are modest for the selected poroelastic parameters, but the addition of elastic effects is shown to reduce the magnitude of the scattered sound. Moreover,
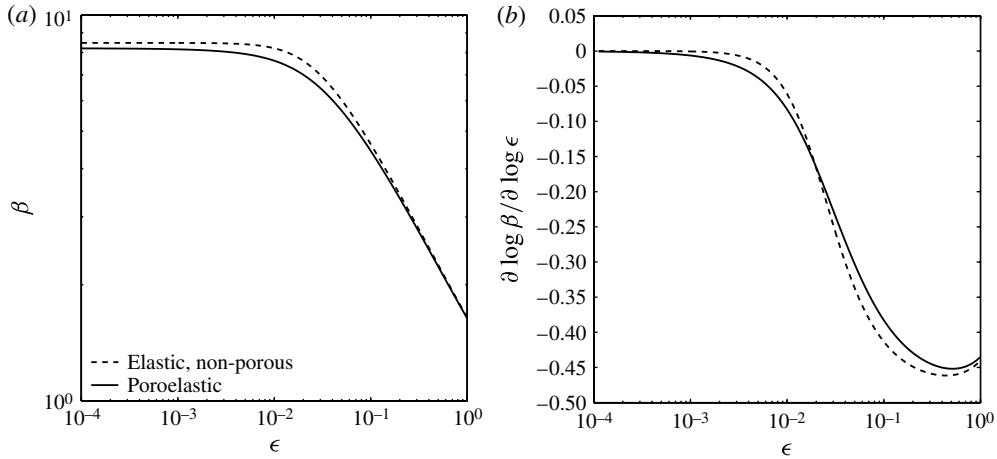
FIGURE 7. Dependence of quadrupole edge noise amplification on the intrinsic fluid loading parameter: (*a*) logarithmic variation; (*b*) slope of logarithmic plot. $\Omega = 0.14$; $\alpha_H = 0.0014$, $R = 0.026$ for the poroelastic case.

the numerical scaling trends replicate the asymptotic result (5.11), where the far-field sound becomes independent of α_H and R when the fractional open area is sufficiently small or the pore size becomes large enough to be on the order of the bending wavelength.

Figure 7 compares the elastic and poroelastic edge amplifications as functions of the intrinsic fluid loading parameter ϵ and implies that edge porosity also diminishes the acoustic intensity in the far field. In conventional aerodynamic applications $\epsilon \sim 10^{-3}$ (see Howe 1998, p. 256), and this small acoustic benefit is predicted to exist; however, in hydrodynamic scenarios $\epsilon \sim 10^{-1}$ and no perceived difference in the radiated intensity would be heard between the elastic and poroelastic cases. The scaling behaviour of the far-field sound on ϵ in figure 7(*b*) exhibits a complicated dependence whose minimum exponent value is in line with the prediction (5.21) for small Ω in the sense that $\Omega \epsilon^{-1/2} \ll 1$, and as $\epsilon \to 0$ the edge becomes effectively rigid and independent of the fluid loading parameter as expected.

The poroelastic model takes advantage of the noise reduction behaviours examined in the above special cases to diminish the amplification of quadrupole sound relative to that of a rigid non-porous edge over a broad range of frequencies. Figure 8 demonstrates that the poroelastic edge behaves like a weakly scattering elastic edge at high and low frequencies, and the effects of porosity are strongest for Ω between 10^{-2} and 10^{-1}. Also, figure 8(*a*) shows that it is the combined effects of the elasticity and porosity of the poroelastic plate that enables its amplification factor to outperform a rigid non-porous edge across the entire frequency range. Figure 9 replots these data as reductions in third-octave sound pressure level measured relative to the rigid non-porous edge as a function of dimensional centre frequency over the range of human hearing. The poroelastic case is again shown to produce the greatest relative reduction of edge noise over all frequencies. The presence of edge elasticity produces a noise-abatement 'bucket' where significant sound reductions occur for high and low frequencies, and a minimum noise reduction exists at a particular frequency whose value depends on porosity. The predicted sharp decline in aerodynamic noise above 1.6 kHz is consistent with existing owl noise measurements (Gruschka, Borchers &
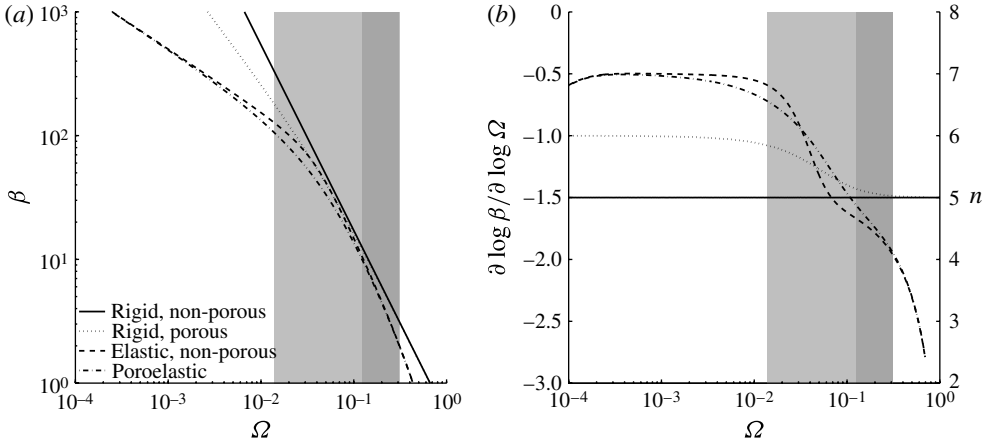
FIGURE 8. Dependence of quadrupole edge noise amplification on the frequency parameter $\Omega = (\omega/\omega_c)^{1/2} = k_0/k_B$: (a) logarithmic variation; (b) slope of logarithmic plot, with n, the exponent of the acoustic power scaling with respect to velocity U, marked on the right-hand vertical axis (i.e. acoustic power U^n). $\epsilon = 0.002$, $\alpha_H = 0.0014$, $R = 0.026$, as required. The shaded regions indicate the hearing range of humans up to 10 kHz, and the darker region denotes the frequency range of interest to the owl, 1.6–10 kHz.
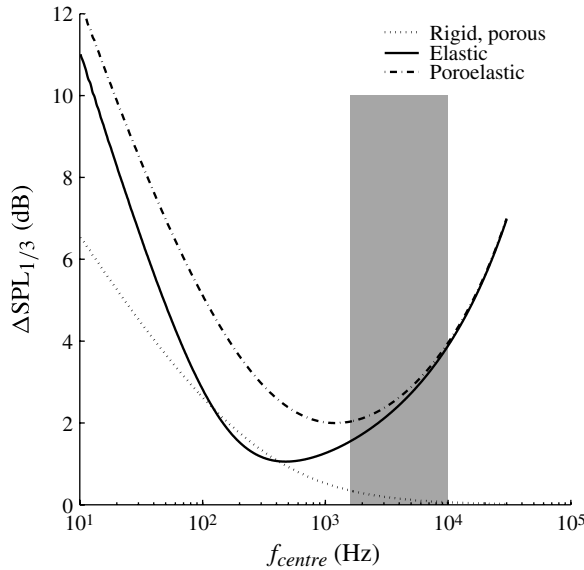

FIGURE 9. Sound pressure level reduction for various edge conditions relative to rigid non-porous trailing-edge noise. Results are reported in third-octave bands as a function of centre frequency over the nominal range of human hearing. The shaded region indicates the frequency range of interest to the owl, 1.6–10 kHz.

Coble 1971), but results from the trailing-edge brush experiment by Herr (2007) resemble instead the behaviour of the rigid and porous edge, where the relative noise reductions predicted at low frequencies diminish asymptotically to zero with increasing frequency.

The velocity scalings indicated in figure 8(*b*) are determined from the logarithmic slope of Ω in β and confirm the regions of fifth-, sixth- and seventh-power dependences predicted analytically in § 5 for rigid, porous, and elastic cases, respectively. Figures 8(*b*) and 9 support the claim that acoustic power scalings with higher exponents of velocity ensure significant noise reductions at low frequency. However, it is important to note that the elastic and poroelastic edges produce larger noise reductions of higher-frequency sound in figure 9 where one might expect an amplification instead from figure 8(*b*) when the velocity exponent falls below the rigid non-porous value of 5. Therefore, the velocity exponent of the acoustic power scaling indicates the potential for significant edge noise reduction, but the amplification factor β is the true metric for sound level comparison.

For polypropylene fibres in air, the frequency range of interest to the owl (1.6–10 kHz) is $0.1242 < \Omega < 0.3104$, where the predicted velocity scaling goes like $U^{4.5-5}$ in agreement with the measurements of Herr (2007). An improvement in noise level is achieved in that study despite retaining approximately the same U^5 noise scaling, but the present theory suggests that U^6 or U^7 behaviours are accessible at the lower end of the human hearing range. Indeed, the theoretical model further implies that the edge properties may be tailored to extend noise reduction benefits to a larger bandwidth of human hearing. The practical goal here is to use porous and elastic treatments to get as close to a sixth-power velocity dependence as possible to diminish edge effects to the point that the scattered sound is of the same order of magnitude as unavoidable noise contributions such as roughness noise, which scales as U^6 like an acoustic dipole (Howe 1984). Recent noise measurements by Geyer, Sarradj & Fritzsche (2010, figure 12) for aerofoils constructed entirely from porous materials indicate that velocity exponents greater than 5 are indeed possible and motivate an extension of the present inviscid analysis to furnish direct comparison with data characterized by viscous flow resistivity.

7. Conclusions

The aerodynamic noise due to a turbulent eddy near a porous and compliant edge is modelled as an acoustic scattering problem involving a semi-infinite poroelastic plate. The Wiener–Hopf technique solves this problem exactly over a range of porosity, intrinsic fluid loading, and frequency parameters, and the essential multiplicative kernel splitting is performed numerically in general and asymptotically for the special cases of porous–rigid and impermeable–elastic edges. The asymptotic factorization furnishes parameter regimes that identify the scaling behaviour of the far-field sound, including its dependence on flow velocity. Edge porosity is shown to modify the radiated acoustic power to a sixth-power velocity dependence, as compared to the well-known fifth-power scaling for an impermeable rigid edge, for sufficiently low frequencies of the turbulent quadrupole. An elastic edge is demonstrated to have a weaker seventh-power dependence on velocity across a finite low-frequency range that is determined numerically. The combined effects of elasticity and porosity are shown to produce the weakest edge amplification but no appreciable change in the velocity exponent over the frequency range of interest to the owl noise problem using a particular set of edge parameters. Consideration of the human hearing range suggests that velocity exponents of 6 or greater are accessible for the poroelastic edge at low frequencies, and that the edge properties may be tailored to yield enhanced noise reduction over a broader frequency range of human audition.

Owl species	Chord (mm)	Wavelengths per chord	Source
Snowy, *Bubo scandiacus*	407.5	1.90	Godfrey & Crosby (1986)
Great grey, *Strix nebulosa*	404.5	1.89	Bull & Duncan (1993)
Great horned, *Bubo virginianus*	340.4	1.59	Earhart & Johnson (1970)
Barred, *Strix varia*	327.8	1.53	Carpenter (1992)
Barn, *Tyto alba*	327.2	1.53	Marti (1990)
Long-eared, *Asio otus*	281.0	1.31	Earhart & Johnson (1970)
Tengmalm's, *Aegolius funereus*	172.5	0.80	Hayward & Hayward (1991)
Burrowing, *Athene cunicularia*	163.0	0.76	Snyder & Wiley (1976)
Northern saw-whet, *Aegolius acadicus*	137.3	0.64	Rains (1998)
Flammulated, *Otus flammeolus*	131.9	0.62	Earhart & Johnson (1970)
Elf, *Micrathene whitneyi*	105.6	0.49	Earhart & Johnson (1970)
Northern pygmy, *Glaucidium gnoma*	90.8	0.42	Snyder & Wiley (1976)

TABLE 1. Wing chord-lengths for various owl species and their magnitudes relative to an acoustic wavelength at frequency 1.6 kHz in air. Representative chord values are the mean of adult male specimens reported in the indicated references.

The validity of the present model for application to fluid-loaded edges requires that the acoustic frequencies of interest are sufficiently large such that the characteristic edge length may be regarded as semi-infinite. For the silent flight of owls, this condition on the model requires the acoustic wavelength of the smallest frequency of interest (1.6 kHz) to be sufficiently short such that the aerofoil chord cannot be regarded as acoustically compact. Table 1 makes this comparison for a representative range of owl sizes suggested by Johnsgard (2002, p. 33). We note that a substantial jump in chord length occurs as it becomes comparable to this critical wavelength (between Tengmalm's owl and the long-eared owl). We further note that the six larger species are well-known silent hunters, and the jump down in wavelengths per chord is accompanied by a change in foraging behaviour to pouncing or surprise attacks from elevated perches and an increase in insect consumption, for which aerodynamic noise suppression is not a tactical priority. Therefore, we argue the validity of our analysis as an idealized model for the trailing-edge noise of the owl based on table 1, and we further speculate that the acoustical non-compactness of the wing with respect to its self-noise signature is an important feature of the owl 'hush-kit'.

We should mention a number of features present in owl and engineered wings but that are absent in the theoretical model, including details of the trailing-edge geometry such as edge thickness (Crighton & Leppington 1973) and serrations (Howe 1991*a*,*b*), as well as viscous fluid action within the poroelastic surface. Of course, for other applications, such as wind turbines, finite chord effects may well be important, especially at lower frequencies, and in that case the use of methods such as described by Amiet (1975), Martinez & Widnall (1980), Howe (2001) and Roger & Moreau (2005) could be very appropriate. Further work is expected to address these effects to

better explain their role in biological aeroacoustics and how such technology can be employed to reduce or effectively eliminate edge noise.

Acknowledgements

Appendix A. Edge conditions and numerical factorization procedure

The requirement of a removable singularity at $\alpha = \alpha_1$ leads to a linear equation of the form

$$F_3 \frac{\partial^3 \eta(0)}{\partial x^3} + F_2 \frac{\partial^2 \eta(0)}{\partial x^2} + F_1 \frac{\partial \eta(0)}{\partial x} + F_0 \eta(0) = F_{RHS}, \tag{A 1}$$

and the same requirement for $\alpha = -\alpha_2$ yields

$$G_3 \frac{\partial^3 \eta(0)}{\partial x^3} + G_2 \frac{\partial^2 \eta(0)}{\partial x^2} + G_1 \frac{\partial \eta(0)}{\partial x} + G_0 \eta(0) = G_{RHS}. \tag{A 2}$$

The coefficients in these equations are:

$$F_3 = -4\alpha_1\alpha_2 K_+(-\alpha_1)K_+(\alpha_2) + I_+(\alpha_1)\left[\alpha_2(\alpha_1 - \alpha_2)K_+(\alpha_2) + 2\alpha_1^2 K_+(-\alpha_1)\right], \tag{A 3}$$

$$F_2 = i\alpha_1\alpha_2 \{4\alpha_1 K_+(-\alpha_1)K_+(\alpha_2) - I_+(\alpha_1)[2\alpha_1 K_+(-\alpha_1) - (\alpha_1 - \alpha_2)K_+(\alpha_2)]\}, \tag{A 4}$$

$$F_1 = -4\alpha_1\alpha_2^3 K_+(-\alpha_1)K_+(\alpha_2) + I_+(\alpha_1)\left[\alpha_2^3(\alpha_1 - \alpha_2)K_+(\alpha_2) + 2\alpha_1^4 K_+(-\alpha_1)\right], \tag{A 5}$$

$$F_0 = i\alpha_1\alpha_2 \left\{4\alpha_1\alpha_2^2 K_+(-\alpha_1)K_+(\alpha_2) + I_+(\alpha_1)\left[\alpha_2^2(\alpha_1 - \alpha_2)K_+(\alpha_2) - 2\alpha_1^3 K_+(-\alpha_1)\right]\right\}, \tag{A 6}$$

$$F_{RHS} = \frac{8ik\sin\theta_0 \, \alpha_1^2\alpha_2(\alpha_1 - \alpha_2)K_+(-\alpha_1)K_+(\alpha_2)I_+(\alpha_1)}{(1 - \alpha_H)\Omega^2 K_+(k\cos\theta_0)(\alpha_1 - k\cos\theta_0)}, \tag{A 7}$$

$$G_3 = -4\alpha_1\alpha_2 K_+(-\alpha_1)K_+(\alpha_2) - I_+(-\alpha_2)\left[2\alpha_2^2 K_+(\alpha_2) - \alpha_1(\alpha_1 - \alpha_2)K_+(-\alpha_1)\right], \tag{A 8}$$

$$G_2 = -i\alpha_1\alpha_2 \{4\alpha_2 K_+(-\alpha_1)K_+(\alpha_2) + I_+(-\alpha_2)[(\alpha_1 - \alpha_2)K_+(-\alpha_1) + 2\alpha_2 K_+(\alpha_2)]\}, \tag{A 9}$$

$$G_1 = -4\alpha_1^3\alpha_2 K_+(-\alpha_1)K_+(\alpha_2) - I_+(-\alpha_2)\left[2\alpha_2^4 K_+(\alpha_2) - \alpha_1^3(\alpha_1 - \alpha_2)K_+(-\alpha_1)\right], \tag{A 10}$$

$$G_0 = i\alpha_1\alpha_2 \left\{4\alpha_1\alpha_2^2 K_+(-\alpha_1)K_+(\alpha_2) - I_+(-\alpha_2)\left[2\alpha_2^3 K_+(\alpha_2) + \alpha_1^2(\alpha_1 - \alpha_2)K_+(-\alpha_1)\right]\right\}, \tag{A 11}$$

$$G_{RHS} = \frac{8ik\sin\theta_0 \, \alpha_1\alpha_2^2(\alpha_1 - \alpha_2)K_+(-\alpha_1)K_+(\alpha_2)I_+(-\alpha_2)}{(1 - \alpha_H)\Omega^2 K_+(k\cos\theta_0)(\alpha_2 + k\cos\theta_0)}. \tag{A 12}$$

The terms involving $K_+(\alpha)$ and $I_+(\alpha)$ are evaluated using the numerical factorization procedure detailed by Peake (2004) and Veitch & Peake (2008). As noted in § 4, the kernel $K(\alpha)$ can be rewritten as $K(\alpha) = \gamma(\alpha)J(\alpha)$, where we require $J(\alpha) \to 1$ as $|\alpha| \to \infty$. Therefore, $K_+(\alpha) = (\alpha + k)^{1/2}J_+(\alpha)$, where

$$J_+(\alpha) = \exp\left[\frac{1}{2\pi i} \int_{\mathscr{C}} \frac{\ln J(\xi)}{\xi - \alpha} \, d\xi\right]. \tag{A 13}$$

The integration contour $\mathscr{C}$ extends from $-\infty$ to $+\infty$ on the real axis, deformed to avoid the branch cuts $\pm k$ to $\pm k \pm i\infty$. Rienstra (2007) has suggested the following parameterization of the complex integration contour:

$$\xi(t) = t + C - \frac{4i\mathscr{D}(t/\mathscr{W})}{3 + (t/\mathscr{W})^4}, \quad -\infty < t < \infty, \tag{A 14}$$

where the parameters C, $\mathscr{D}$ and $\mathscr{W}$ are suitably chosen to obey the restrictions outlined above. The resulting infinite integral can be mapped to a finite integral by a change of variables, $t(s) = s/(1 - s^2)^2$, and evaluated for any chosen α using standard quadrature routines.

Greater care must be taken when evaluating $I_+(\alpha)$ at $\alpha = \alpha_1$ or $\alpha = -\alpha_2$, where the numerical factorization procedure requires a function that approaches unity as $|\alpha| \to \infty$. To achieve this for the case of $\alpha = \alpha_1$, introduce the term $(\alpha^2 + \zeta^2)$, where ζ is a prescribed positive real number. Equation (4.13) can then be rearranged into

$$I(\alpha) = \gamma(\alpha)(\alpha^2 - \alpha_2^2)(\alpha^2 + \zeta^2)P(\alpha), \tag{A 15}$$

where $P(\alpha) \to 1$ as $|\alpha| \to \infty$. This expression can then be factored to produce

$$I_+(\alpha_1) = (\alpha_1 + \alpha_2)(\alpha_1 + i\zeta)(\alpha_1 + k)^{1/2} P_+(\alpha_1), \tag{A 16}$$

and $P_+(\alpha_1)$ is determined numerically in the same manner as (A 13). The same procedure can be applied for $\alpha = -\alpha_2$ to get

$$I(\alpha) = \gamma(\alpha)(\alpha^2 - \alpha_1^2)(\alpha^2 + \zeta^2)Q(\alpha), \tag{A 17}$$

$$I_+(-\alpha_2) = -(\alpha_1 + \alpha_2)(-\alpha_2 + i\zeta)(-\alpha_2 + k)^{1/2} Q_+(-\alpha_2). \tag{A 18}$$

Appendix B. Asymptotic evaluation of elastic-edge kernel

The multiplicative factorization of (5.13) for $\kappa_1 \ll 1$ proceeds from the fact that the perturbed kernel may be written in the following manner (Cannell 1975; Noble 1988):

$$\begin{aligned} K(\alpha, \kappa_1) &= \left(K_-^{(0)} - \kappa_1 K_-^{(1)} + o(\kappa_1)\right)\left(K_+^{(0)} - \kappa_1 K_+^{(1)} + o(\kappa_1)\right) \\ &= K_-^{(0)}K_+^{(0)} - \kappa_1\left(K_-^{(0)}K_+^{(1)} + K_+^{(0)}K_-^{(1)}\right) + O(\kappa_1^2) \\ &= K^{(0)}(\alpha) - \kappa_1 K^{(1)}(\alpha) \\ &= (\alpha^2 - k^2)^{1/2} - \kappa_1(\alpha^2 - \alpha_1^2)^{-1}(\alpha^2 - \alpha_2^2)^{-1}. \end{aligned} \tag{B 1}$$

Equating the coefficients of the last two lines leads first to $K^{(0)}(\alpha) = K_-^{(0)}K_+^{(0)} = (\alpha^2 - k^2)^{1/2}$. Thus, $K_\pm^{(0)}(\alpha) = b_0^{\pm 1}(\alpha \pm k)^{1/2}$, where b_0 is a complex constant. Secondly, a Wiener–Hopf equation emerges for $K^{(1)}(\alpha)$:

$$\frac{K_+^{(1)}}{K_+^{(1)}} + \frac{K_-^{(1)}}{K_-^{(1)}} = \frac{K^{(1)}}{K_+^{(0)}}, \tag{B 2}$$

where

$$\frac{K^{(1)}}{K_+^{(0)}} = (\alpha^2 - \alpha_1^2)^{-1}(\alpha^2 - \alpha_2^2)^{-1}(\alpha^2 - k^2)^{-1/2}. \tag{B 3}$$

The additive factorization of $(\alpha^2 - k^2)^{-1/2} = T_-(\alpha) + T_+(\alpha)$ is (Noble 1988, p. 21)

$$T_\pm(\alpha) = \frac{1}{\pi(\alpha^2 - k^2)^{1/2}} \arccos\left(\pm\frac{\alpha}{k}\right). \tag{B 4}$$

Elementary pole removals enable the additive factorization of $K^{(1)}/K_+^{(0)} = F_- + F_+$, and the usual analytical continuation arguments for problems of this type lead to

$$K_+(\alpha) = (\alpha + k)^{1/2}(1 - \kappa_1 F_+(\alpha) + o(\kappa_1)), \tag{B 5}$$

$$F_\pm(\alpha) = \frac{T_\pm(\alpha)}{(\alpha^2 - \alpha_1^2)(\alpha^2 - \alpha_2^2)} \mp \left\{ \frac{T_+(-\alpha_1)}{4\alpha_1(\alpha + \alpha_1)} + \frac{T_-(\alpha_1)}{4\alpha_1(\alpha - \alpha_1)} \right.$$
$$\left. + \frac{T_-(-\alpha_2)}{4\alpha_2(\alpha + \alpha_2)} + \frac{T_+(\alpha_2)}{4\alpha_2(\alpha - \alpha_2)} \right\}. \tag{B 6}$$

Thus, $K_+(k\cos\theta_0) \sim \Omega^{1/2}$ for $\kappa_1 \ll 1$.

REFERENCES

AMIET, R. K. 1975 Acoustic radiation from an airfoil in a turbulent stream. *J. Sound Vib.* **41** (4), 407–420.

BARONE, J. R. & SCHMIDT, W. F. 2005 Polyethylene reinforced with keratin fibres obtained from chicken feathers. *Compos. Sci. Technol.* **65**, 173–181.

BATCHELOR, G. K. 1967 *An Introduction to Fluid Dynamics*. Cambridge University Press.

BERS, A. 1983 Space–time evolution of plasma instabilities – absolute and convective. In *Basic Plasma Physics* (ed. A. A. Galeev & R. N. Sudan), Handbook of Plasma Physics, vol. 1, North-Holland.

BLISS, D. B. 1982 Study of bulk reacting porous sound absorbers and a new boundary condition for thin porous layers. *J. Acoust. Soc. Am.* **71** (3), 533–545.

BONSER, R. & PURSLOW, P. 1995 The Young's modulus of feather keratin. *J. Expl Biol.* **198**, 1029–1033.

BRIGGS, R. J. 1964 *Electron-Stream Interaction with Plasmas*. MIT.

BULL, E. L. & DUNCAN, J. R. 1993 *Great Gray Owl: Strix Nebulosa*. American Orinthologists' Union.

CANNELL, P. A. 1975 Edge scattering of aerodynamic sound by a lightly loaded elastic half-plane. *Proc. R. Soc. Lond.* A **347** (1649), 213–238.

CANNELL, P. A. 1976 Acoustic edge scattering by a heavily loaded elastic half-plane. *Proc. R. Soc. Lond.* A **350** (1660), 71–89.

CARPENTER, T. W. 1992 Utility of wing length, tail length and tail barring in determining the sex of Barred Owls collected in Michigan and Minnesota. *The Condor* **94**, 794–795.

CHONG, T. P., JOSEPH, P. F. & GRUBER, M. 2013 Airfoil self noise reduction by non-flat plate type trailing edge serrations. *Appl. Acoust.* **74**, 607–613.

CRIGHTON, D. G. 1972 Acoustic edge scattering of elastic surface waves. *J. Sound Vib.* **22** (1), 25–32.

CRIGHTON, D. G. 1991 Airframe noise. In *Aerodynamic Theory: A General Review of Progress. Volume 1: Noise Sources* (ed. H. H. Hubbard). NASA Langley Research Center.

CRIGHTON, D. G. 2001 Asymptotic factorization of Wiener–Hopf kernels. *Wave Motion* **33**, 51–65.

CRIGHTON, D. G. & LEPPINGTON, F. G. 1970 Scattering of aerodynamic noise by a semi-infinite compliant plate. *J. Fluid Mech.* **43** (4), 721–736.

CRIGHTON, D. G. & LEPPINGTON, F. G. 1973 Singular perturbation methods in acoustics: diffraction by a plate of finite thickness. *Proc. R. Soc. Lond.* A **335** (1602), 313–339.

CURLE, N. 1955 The influence of solid boundaries upon aerodynamic sound. *Proc. R. Soc. Lond.* A **231** (1187), 505–514.

DASSEN, T., PARCHEN, R., BRUGGEMAN, J. & HAGG, F. 1996 Results of a wind tunnel study on the reduction of airfoil self-noise by the application of serrated blade trailing edges. In *European Union Wind Energy Conference and Exhibition, Gothenburg, Sweden*, pp. 800–803.

EARHART, C. M. & JOHNSON, N. K. 1970 Size dimorphism and food habits of North American owls. *The Condor* **72**, 251–264.

FFOWCS WILLIAMS, J. E. 1972 The acoustics of turbulence near sound-absorbent liners. *J. Fluid Mech.* **51** (4), 737–749.

FFOWCS WILLIAMS, J. E. & HALL, L. E. 1970 Aerodynamic sound generation by turbulent flow in the vicinity of a scattering half plane. *J. Fluid Mech.* **40** (4), 657–670.

GEYER, T., SARRADJ, E. & FRITZSCHE, C. 2010 Measurement of the noise generation at the trailing edge of porous airfoils. *Exp. Fluids* **48** (2), 291–308.

GODFREY, W. E. & CROSBY, J. A. 1986 *The Birds of Canada*. National Museum of Natural Sciences.

GRAHAM, R. R. 1934 The silent flight of owls. *J. R. Aero. Soc.* **38**, 837–843.

GRUSCHKA, H. D., BORCHERS, I. U. & COBLE, J. G. 1971 Aerodynamic noise produced by a gliding owl. *Nature* **233**, 409–411.

HAYDEN, R. E. 1976 Reduction of noise from airfoils and propulsive lift systems using variable impedance systems. *AIAA Paper* 1976-500.

HAYWARD, G. D. & HAYWARD, P. H. 1991 Body measurements of Boreal Owls in Idaho and a discriminant model to determine sex of live specimens. *Wilson Bull.* **103** (3), 497–500.

HERR, M. 2007 Design criteria for low-noise trailing-edges. *AIAA Paper* 2007-3470.

HERR, M. & DOBRZYNSKI, W. 2005 Experimental investigations in low-noise trailing-edge design. *AIAA J.* **43** (6), 1167–1175.

HOWE, M. S. 1978 A review of the theory of trailing edge noise. *J. Sound Vib.* **61** (3), 437–465.

HOWE, M. S. 1979*a* On the added mass of a perforated shell, with application to the generation of aerodynamic sound by a perforated trailing edge. *Proc. R. Soc. Lond.* A **365** (1721), 209–233.

HOWE, M. S. 1979*b* On the theory of unsteady high Reynolds number flow through a circular aperture. *Proc. R. Soc. Lond.* A **366** (1725), 205–223.

HOWE, M. S. 1984 On the generation of sound by turbulent boundary layer flow over a rough wall. *Proc. R. Soc. Lond.* A **395** (1809), 247–263.

HOWE, M. S. 1991*a* Aerodynamic noise of a serrated trailing edge. *J. Fluids Struct.* **5** (1), 33–45.

HOWE, M. S. 1991*b* Noise produced by a sawtooth trailing edge. *J. Acoust. Soc. Am.* **90** (1), 482–487.

HOWE, M. S. 1992 Sound produced by an aerodynamic source adjacent to a partly coated, finite elastic plate. *Proc. R. Soc. Lond.* A **436** (1897), 351–372.

HOWE, M. S. 1993 Structural and acoustic noise produced by turbulent flow over an elastic trailing edge. *Proc. R. Soc. Lond.* A **442** (1916), 533–554.

HOWE, M. S. 1998 *Acoustics of Fluid-Structure Interactions*. Cambridge University Press.

HOWE, M. S. 2001 Edge-source acoustic Green's function for an airfoil of arbitrary chord, with application to trailing-edge noise. *Q. J. Mech. Appl. Maths* **54** (1), 139–155.

HOWE, M. S., SCOTT, M. I. & SIPCIC, S. R. 1996 The influence of tangential mean flow on the Rayleigh conductivity of an aperture. *Proc. R. Soc. Lond.* A **452** (1953), 2303–2317.

HUGHES, I. J. & DOWLING, A. P. 1990 The absorption of sound by perforated linings. *J. Fluid Mech.* **218**, 299–335.

JOHNSGARD, P. A. 2002 *North American Owls: Biology and Natural History*, 2nd edn. Smithsonian Institution.

JONES, L. E. & SANDBERG, R. D. 2012 Acoustic and hydrodynamic analysis of the flow around an aerofoil with trailing-edge serrations. *J. Fluid Mech.* **706**, 295–322.

KHORRAMI, M. R. & CHOUDHARI, M. M. 2003 Application of passive porous treatment for slat trailing edge noise. *NASA Tech. Rep.* TM-2003-212416.

KRANZER, H. C. 1968 Asymptotic factorization in nondissipative Wiener–Hopf problems. *J. Math. Mech.* **17**, 577–600.

KRANZER, H. C. & RADLOW, J. 1962 Asymptotic factorization for perturbed Wiener–Hopf problems. *J. Math. Anal. Appl.* **4**, 240–256.

KRANZER, H. C. & RADLOW, J. 1965 An asymptotic method for solving perturbed Wiener–Hopf problems. *J. Math. Mech.* **14**, 41–59.

KROEGER, R. A., GRUSCHKA, H. D. & HELVEY, T. C. 1972 Low speed aerodynamics for ultra-quiet flight. *Tech. Rep.* AFFDL-TR-71-75. Air Force Flight Dynamics Laboratory, Wright-Patterson AFB.

LEPPINGTON, F. G. 1977 The effective compliance of perforated screens. *Mathematika* **24**, 199–215.

LEPPINGTON, F. G. 1990 The effective boundary conditions for a perforated elastic sandwich panel in a compressible fluid. *Proc. R. Soc. Lond.* A **427** (1873), 385–399.

LIGHTHILL, M. J. 1952 On sound generated aerodynamically. Part 1. General theory. *Proc. R. Soc. Lond.* A **211** (1107), 564–587.

LILLEY, G. M. 1998 A study of the silent flight of the owl. *AIAA Paper* 1998-2340.

MARTI, C. D. 1990 Sex and age dimorphism in the Barn Owl and a test of mate choice. *The Auk* **107**, 246–254.

MARTINEZ, R. & WIDNALL, S. E. 1980 Unified aerodynamic-acoustic theory for a thin rectangular wing encountering a gust. *AIAA J.* **18** (6), 636–645.

MOREAU, D. J., BROOKS, L. A. & DOOLAN, C. J. 2012 On the noise reduction mechanism of a flat plate serrated trailing edge at low-to-moderate Reynolds number. *AIAA Paper* 2012-2186.

NELSON, P. A. 1982 Noise generated by flow over perforated surfaces. *J. Sound Vib.* **83** (1), 11–26.

NOBLE, B. 1988 *Methods Based on the Wiener–Hopf Technique for the Solution of Partial Differential Equations*. Chelsea.

OERLEMANS, S., FISHER, M., MAEDER, T. & KÖGLER, K. 2009 Reduction of wind turbine noise using optimized airfoils and trailing-edge serrations. *AIAA J.* **47** (6), 1470–1481.

PEAKE, N. 2004 On the unsteady motion of a long fluid-loaded elastic plate with mean flow. *J. Fluid Mech.* **507**, 335–366.

RAINS, C. R. 1998 Niche overlap, and nearest-neighbor distances of Northern Saw-whet Owls (*aegolius acadicus*) and Western Screech-owls (*otus kennicottii*) in southwestern Idaho. PhD thesis, Boise State University.

RAYLEIGH, LORD 1945 *The Theory of Sound*, vol. 2. Dover.

RIENSTRA, S. W. 2007 Acoustic scattering at a hard-soft lining transition in a flow duct. *J. Engng Maths* **59** (4), 451–475.

ROGER, M. & MOREAU, S. 2005 Back-scattering correction and further extensions of Amiet's trailing-edge noise model. Part 1. Theory. *J. Sound Vib.* **286**, 477–506.

SANDBERG, R. D. & JONES, L. E. 2011 Direct numerical simulations of low Reynolds number flow over airfoils with trailing-edge serrations. *J. Sound Vib.* **330**, 3818–3831.

SARRADJ, E., FRITZSCHE, C. & GEYER, T. 2011 Silent owl flight: flyover noise measurements. *AIAA J.* **49** (4), 769–779.

SNYDER, N. F. & WILEY, J. W. 1976 *Sexual Size Dimorphism in Hawks and Owls of North America (No. 20)*. American Orinthologists' Union.

TIMOSHENKO, S. 1940 *Theory of Plates and Shells*, 1st edn. McGraw-Hill.

VAN DYKE, M. 1975 *Perturbation Methods in Fluid Mechanics*. Parabolic.

VEITCH, B. & PEAKE, N. 2008 Acoustic propagation and scattering in the exhaust flow from coaxial cylinders. *J. Fluid Mech.* **613**, 275–307.

ZWIKKER, C. & KOSTEN, C. W. 1949 *Sound Absorbing Materials*. Elsevier.